ISSN 8756-3282
Volume 50, Issue 3, March 2012

# Bone

ELSEVIER

Available online at www.sciencedirect.com

SciVerse ScienceDirect

Official Journal
International Bone
& Mineral Society

IBMS
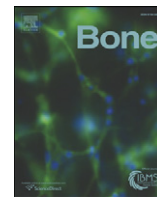
Original Full Length Article

# Further improvements on the factors affecting bone mineral density measured by quantitative micro-computed tomography

Vahid Entezari [a], Vartan Vartanians [a], David Zurakowski [b,c], Nipun Patel [a], Roberto J. Fajardo [e], Ralph Müller [f], Brian D. Snyder [a,d], Ara Nazarian [a,*]

[a] Center for Advanced Orthopedic Studies, Department of Orthopaedic Surgery, Beth Israel Deaconess Medical Center, Harvard Medical School, Boston, MA, USA
[b] Department of Anesthesiology, Children's Hospital, Harvard Medical School, Boston, MA, USA
[c] Department of General Surgery, Children's Hospital, Harvard Medical School, Boston, MA, USA
[d] Department of Orthopaedic Surgery, Children's Hospital, Harvard Medical School, Boston, MA, USA
[e] Department of Orthopaedics, University of Texas Health Science Center at San Antonio, San Antonio, TX, USA
[f] Institute for Biomechanics, ETH Zürich, Zürich, Switzerland

## ARTICLE INFO

## ABSTRACT

The effects of imaging parameters and special configuration of objects within the reconstruction space on the micro computed tomography ($\mu$CT) based mineral density have been explored, and a series of density correction curves have been presented. A manufacturer-provided calibration phantom (0, 100, 200, 400, 800 mg HA/cm$^3$) was imaged at all possible imaging conditions ($n = 216$) based on energy, resolution, vial diameter, beam hardening correction factor and averaging. For each imaging condition, a linear regression model was fitted to the observed versus expected densities, and the intercepts ($\beta_0$) and slopes ($\beta_1$) of the regression lines and each density level were modeled using multiple regression modeling. Additionally, a custom made phantom (0, 50, 150, 500, 800, 1000 and 1500 mg HA/cm$^3$) was scanned in order to study the effects of location and orientation of an object within the reconstruction space and presence of surrounding objects on $\mu$CT based mineral density. The energy, vial diameter and beam hardening correction factor were significant predictors of cumineral density (P values<0.001), while averaging and resolution did not have a significant effect on the observed density values (P values>0.1) except for 0.0 density (P values<0.04). Varying the location of an object within the reconstruction space from the center to the periphery resulted in a drop in observed mineral density up to 10% (P values<0.005). The presence of surrounding densities resulted in decreased observed mineral density up to 17% at the center and up to 14% at the periphery of the reconstruction space (P values<0.001 for all densities). Changing the orientation of the sample also had a significant effect on the observed mineral density, resulting in up to 16% lower observed mineral density for vertical vs. horizontal orientation at the center of the reconstruction space (P value<0.001). We conclude that energy, resolution and post processing correction factor are significant predictors of the observed mineral density in $\mu$CT.

© 2011 Elsevier Inc. All rights reserved.

## Introduction

Micro-computed tomography ($\mu$CT) has been used extensively to generate high-resolution images and microstructural indices of normal and pathologic cortical and trabecular bones. Recently, liquid and solid phantoms have been used to convert X-ray attenuation coefficient to bone mineral density for $\mu$CT systems. Although, the use of phantoms with $\mu$CT imaging has become commonplace, the technical and physical factors that influence the analytic relationship for converting X-ray attenuation coefficients into bone mineral density have only begun to be studied.

In computed tomography the projections from an image are the line integrals of the attenuation coefficient. The beam attenuation is due to absorption of photons by the atoms of the material they are traversing through, or by being scattered away from their original paths. The former mechanism of photon attenuation is the photoelectric effect and the latter the Compton effect. Photoelectric absorption is caused by the X-ray photon imparting all of its energy to a tightly bound inner electron in an atom, whereas, the Campton scatter is due to the interaction of the X-ray photon with either a free electron or one that is loosely bound in one of the outer shells of an atom [1]. Both of these phenomena are photon energy dependent, meaning

* Corresponding author at: Center for Advanced Orthopedic Studies, 330 Brookline Avenue, RN115, Boston, MA 02215, USA. Fax: +1 617 667 7175.
E-mail addresses: ventezar@bidmc.harvard.edu (V. Entezari), vvartanians@partners.org (V. Vartanians), david.zurakowski@childrens.harvard.edu (D. Zurakowski), ndpatel@bidmc.harvard.edu (N. Patel), fajardor@uthscsa.edu (R.J. Fajardo), ram@ethz.ch (R. Müller), brian.snyder@childrens.harvard.edu (B.D. Snyder), anazaria@bidmc.harvard.edu (A. Nazarian).

that the probability of a photon being lost either due to photoelectric absorption or Compton scatter is a function of the photon energy.

The attenuation of mixtures and compounds, as described by the exponential attenuation law for monochromatic beams (single energy photons) and outlined in equation one, is therefore rewritten as Eq. (2):

$$\frac{I}{I_0} = e^{[-\mu x]} \tag{1}$$

$$\mu(E) = \tau(E) + \sigma(E) \tag{2}$$

where $\tau$ and $\sigma$ represent photoelectric and Compton effects respectively. As equation one is only valid for monochromatic beams, and X-ray computed tomography do not produce monochromatic beams, equation one is to be re-written to emphasize the spatial and energy dependence of X-ray attenuation coefficient [1]. The polychromatic nature of the beams used in most diagnostic imaging causes the linear attenuation of many tissues to decrease with energy, mostly due to beam hardening or the preferential absorption of lower energy (softer) beams by the material.

Kazakia et al. have shown that mineral densities obtained by μCT are moderately correlated with ash density values for both cortical and trabecular bone and correlate highly with mineral densities acquired by synchrotron radiation micro-computed tomography (SRμCT) [2]. The authors have previously shown that tube voltage, object to source distance, detector array size and different media surrounding the sample significantly affect the μCT generated X-ray attenuation values of bone [3]. They have also shown that tube current and integration time do not affect the μCT based attenuation values of bone [3]. However, the effects of other factors such as averaging and beam hardening correction factor on the μCT based attenuation values of bone have not been studied before.

Introduction of beam hardening correction algorithms have substantially improved mineral density measurements by μCT; however, as evidenced by recent findings [4,5], residual artifacts must still be contended with. Moreover, current calibration phantoms cover a range of density between 0 and 800 mg HA/cm$^3$, which is reasonable for trabecular bone samples, but most cortical samples from different species lie beyond this range (Fig. 1).

Burghardt et al. reported a large discrepancy in regression equations of μCT based tissue mineral density and ash density between cortical and trabecular samples with different volume fraction [4]. Additionally, Fajardo et al. have shown that specimen size plays a significant role on bone X-ray attenuation values [6]. However, other important factors such as location of an object within the reconstruction space (with respect to the reconstruction center) and presence of

**Table 1**
Definition of the standard, medium and high resolutions.

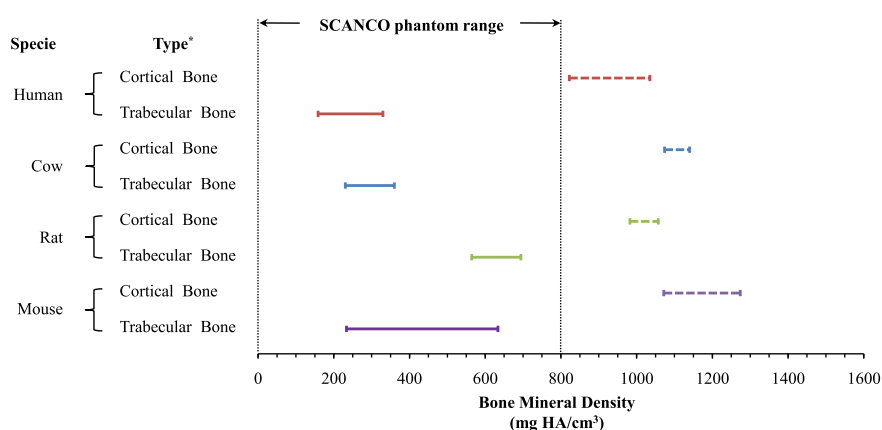| Resolution | Detector size (pixel$^2$) | No. of projection (per 180) | Vial diameter (mm) | Voxel size ($\mu m^3$) |
|---|---|---|---|---|
| Standard | 1024×1024 | 250 | 16.4 | 16 |
| | | | 20.5 | 20 |
| | | | 30.7 | 30 |
| | | | 36.9 | 36 |
| Medium | 1024×1024 | 500 | 16.4 | 16 |
| | | | 20.5 | 20 |
| | | | 30.7 | 30 |
| | | | 36.9 | 36 |
| High | 2048×2048 | 1000 | 16.4 | 8 |
| | | | 20.5 | 10 |
| | | | 30.7 | 15 |
| | | | 36.9 | 18 |

surrounding tissues on bone mineral density measured by μCT have not been evaluated to the best of our knowledge.

Therefore, in order to address these questions, we aim to: 1) investigate the effects of imaging parameters of energy, resolution, vial diameter, averaging and beam hardening correction factor on μCT based bone mineral density; 2) generate a multivariate regression model to further correct bone mineral density measured by μCT based on imaging parameters; and 3) investigate the effects of spatial configuration of objects within the reconstruction space on the μCT based bone mineral density.

## Materials and methods

### Imaging

Solid hydroxyapatite (HA) calibration phantoms (SCANCO), provided by the manufacturer (Scanco Medical AG, Brüttisellen, Switzerland), were used as a surrogate for bone specimens to study the effects of imaging conditions on the observed mineral density (Aim 1) and generate a regression model to correct observed mineral density (Aim 2). SCANCO phantoms consisted of 0, 100, 200, 400 and 800 mg HA/cm$^3$ phantom rods embedded in resin. A 1.6 mm trans-axial section of each phantom was imaged three times using a Scanco 40 system (Scanco Medical AG, Brüttisellen, Switzerland) for all 216 imaging conditions based on five imaging parameters of energy or tube voltage (45, 55 and 70 kVp), scanning resolution (low, medium and high, see Table 1), vial diameter (16.4, 20.5, 30.7 and 36.9 mm), beam hardening correction factor (200, 700 and 1200 mg HA/cm$^3$) and averaging (1 or 2 images). The beam hardening correction factor allows the end user to select one of the three levels of beam hardening corrections (200, 700 or 1200 mg HA/cm$^3$) for each energy level using wedge HA phantoms



**Fig. 1.** The range of μCT-based mineral density of cortical (dashed line) and cancellous bones (solid lines) from different species (mouse, rat, cow and adult human).

*\* Values depicted in this figure are based on μCT scans of 5 representative samples for each specie/bone type*
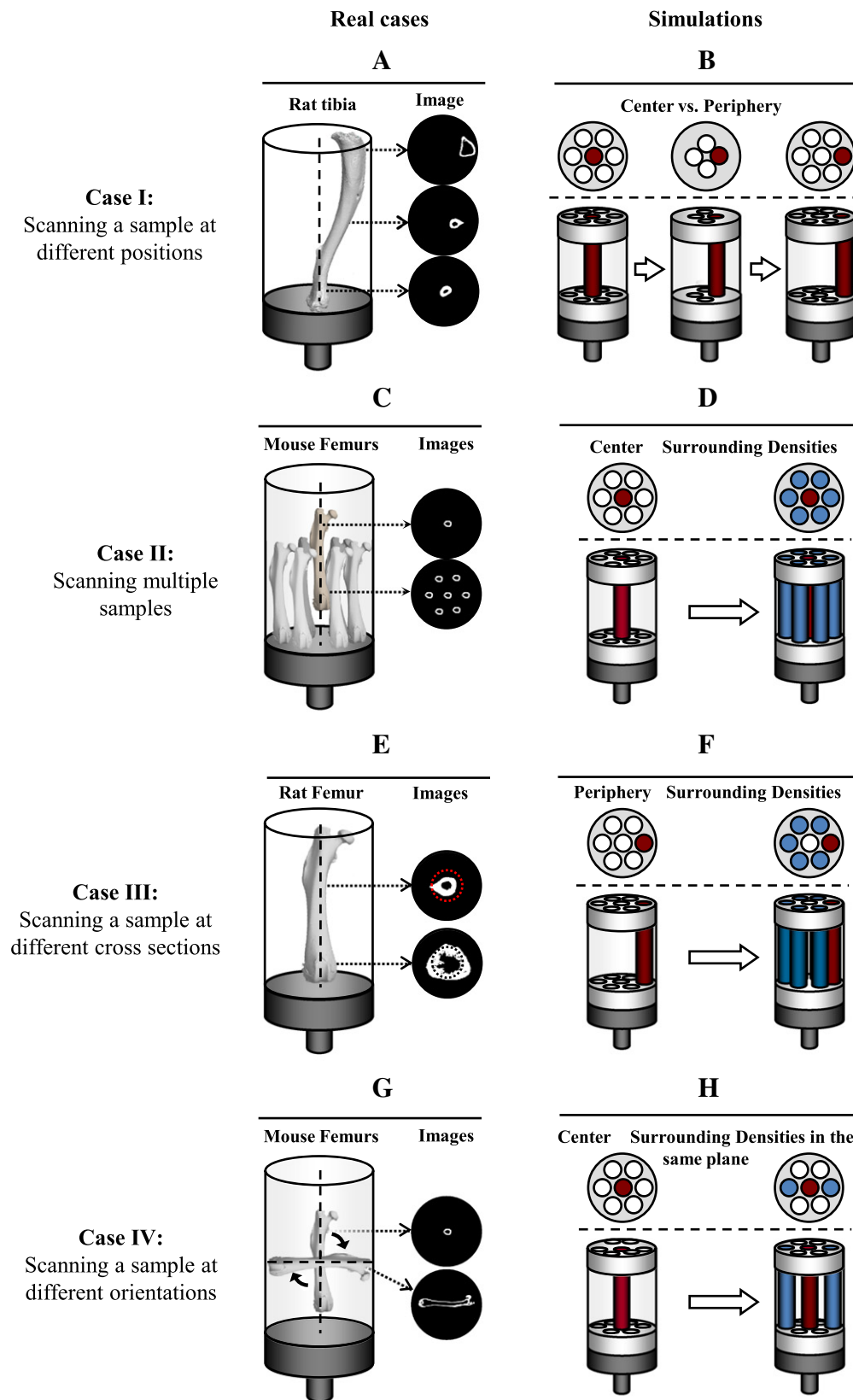
**Fig. 2.** Schematic representation of the imaging set-up (A) and three common imaging scenarios simulated by a set of phantoms. In Case I (center vs. periphery), different cross-sections of a bone with a curvilinear shape is reconstructed either at the center or at the periphery of the reconstruction space (B, C). In Case II (center ± surrounding), the scanning orientation of a long bone will alter the distribution of mineral tissue around the center of the reconstruction space (D, E). In Case III (periphery ± surrounding), scanning bones with different cross sectional geometry leads to different distributions of mineralized tissue from the center of reconstruction space (e.g. rat tibial vs. femoral cortical shell cortex) (F,G).

[7]. Averaging multiplies the integration time data with a factor from 1 to 10 and is useful for non-standard measurements with integration times over the maximum value. The practical drawback of using high averaging factors is in multiplying the scan time by the averaging factor. As a result, we have explored averaging values of 1 and 2 as reasonable and commonly used factors. A circular region of interest at 50% of the diameter of the whole cross-section was selected at the center of each phantom to obtain mean X-ray attenuation coefficient for each phantom. The authors have previously reported the homogeneity of the SCANCO calibration phantoms by scanning each phantom at three different locations (top, middle and bottom) resulting in minimal variation (p = 0.28) [3].

In order to study the effect of spatial configurations on the observed mineral density (Aim 3), an in house phantom holder comprised of phantom rods of 50, 150, 500, 800, 1000 and 1500 mg HA/cm$^3$ (CIRS, Norfolk, VA, USA) (HA.CIRS) surrounded by distilled water in a 16 mm µCT vial was designed and manufactured to allow for changing the position and configurations of phantom rods inside the reconstruction space. Four spatial configurations of phantoms were studied to simulate common scanning scenarios outlined in Cases I through IV.

### Case I: Center vs. periphery

This case studies the effect of moving an object from the center to the periphery of the reconstruction space. An example for this scenario is imaging of a bone with a curvilinear shape (e.g. rat tibia) at the longitudinal direction (Fig. 2A) or scanning specimens at different distances from the reconstruction center. As a result of the asymmetric longitudinal geometry of the bone relative to the vertical axis of the reconstruction space, cross-sections of the bone will be reconstructed either at the center or at the periphery of the reconstruction space. To simulate this scenario, three phantoms rods with densities of 500, 1000 and 1500 mg HA/cm$^3$, representing the typical range of bone mineral density, were scanned each at the center and two peripheral points at 6.92 and 12.17 mm from the center of the reconstruction space (Fig. 2B).

### Case II: Center ± surrounding densities

This case aims to study the effect of surrounding densities on the µCT based attenuation values of an object at the center of the reconstruction space. For instance, scanning multiple specimens at the same cross-section will affect the observed mineral density at the center of the reconstruction space (Fig. 2C). In order to simulate this scenario, three phantom rods with densities of 500, 1000 and 1500 mg HA/cm$^3$ were scanned each at the center of the vial with

and without six surrounding phantom rods with densities of 50, 150, 500, 800, 1000 and 1500 mg HA/cm$^3$ at 4.65 mm from the center of the reconstruction space (Fig. 2D).

### Case III: Periphery ± surrounding densities

This case simulates the effect of the presence or absence of surrounding densities on the µCT-based attenuation values of an object at the periphery of the reconstruction space. For instance, µCT imaging of a distal diaphyseal cross-section of the femur will result in relatively uniform distribution of density relative to the center of the reconstruction space, while metaphyseal cross section of the same bone will result in a non-uniform distribution of the mineralized tissue (Fig. 2E). If one were to consider a voxel from femoral diaphysis with a circular cross-section, each voxel will be surrounded by a range of densities which are at the same distance from the reconstruction center (red dots), as opposed to a point at the edge of the femoral metaphysis with a more triangular cross-section, which will be surrounded by smaller amount of densities equidistant from the reconstruction center (white dotes). To test this scenario, three phantom rods with densities of 500, 1000 and 1500 mg HA/cm$^3$ were scanned each at 4.65 mm from the center of the reconstruction space with and without five surrounding phantom rods with densities of 50, 150, 500, 800, 1000 and 1500 mg HA/cm$^3$ at the same distance from the center of the reconstruction space (Fig. 2F).

### Case IV: Vertical vs. horizontal orientation

This case aims to study the effect of sample orientation on the µCT based attenuation values of an object at the center of the reconstruction space. For instance, scanning orientation of a long bone (perpendicular or parallel to the long axis of the bone) will alter the distribution of mineral tissue around the center of the reconstruction space (Fig. 2G). In order to simulate this scenario, three phantom rods with densities of 500, 1000 and 1500 mg HA/cm$^3$ were scanned each at the center of the vial with and without two surrounding phantom rods with the same densities at 4.65 mm from the center of the reconstruction space to represent spreading of densities in a single plane, when a long bone is moved from vertical to horizontal orientation (Fig. 2H).

### Statistical analysis

For Aim 1, the apparent mineral density as reported by the manufacturer was considered the expected mineral density ($\rho_{EXP}$) for each phantom rod. In order to study the effect of imaging condition on the

**Table 2**
The effect of different imaging conditions on the observed mineral density of the SCANCO phantoms.

| $\rho_{EXP}$ (mg HA/cm$^3$) | $\rho_{OBS}$ (mg HA/cm$^3$) | | | | | | | | | | | | | | |
|---|---|---|---|---|---|---|---|---|---|---|---|---|---|---|
| | Energy (Kvp) | | | Resolution | | | Vial diameter (mm) | | | | Beam hardening correction factor (mg HA/com$^3$) | | | Averaging | |
| | 45 | 55 | 70 | Low | Medium | High | 16.4 | 20.5 | 30.7 | 36.9 | 200 | 700 | 1200 | 1 image | 2 images |
| | Mean | Mean | Mean | Mean | Mean | Mean | Mean | Mean | Mean | Mean | Mean | Mean | Mean | Mean | Mean |
| | SD | SD | SD | SD | SD | SD | SD | SD | SD | SD | SD | SD | SD | SD | SD |
| 0 | −30.0 | −32.2 | −37.3 | −32.9 | −33.7 | −32.9 | −31.3 | −33.0 | −33.2 | −35.1 | −24.9 | −35.4 | −39.2 | −32.7 | −33.6 |
| | 5.5 | 5.5 | 8.4 | 7.3 | 7.3 | 7.3 | 7.0 | 7.5 | 7.3 | 7.1 | 2.5 | 4.4 | 5.0 | 7.3 | 7.3 |
| 100 | 84.3 | 83.2 | 76.2 | 81.5 | 81.3 | 80.8 | 83.4 | 82.8 | 80.9 | 77.7 | 99.7 | 75.0 | 69.0 | 81.4 | 81.0 |
| | 11.9 | 11.6 | 17.6 | 14.4 | 14.4 | 14.5 | 14.4 | 14.2 | 14.2 | 14.2 | 2.6 | 4.4 | 7.7 | 14.4 | 14.4 |
| 200 | 209.5 | 212.7 | 207.5 | 210.6 | 209.9 | 209.1 | 212.6 | 212.8 | 210.2 | 203.9 | 238.2 | 199.7 | 191.8 | 210.7 | 209.1 |
| | 18.6 | 18.0 | 26.4 | 21.3 | 21.3 | 21.8 | 22.0 | 21.1 | 21.0 | 20.8 | 5.5 | 4.6 | 9.0 | 21.3 | 21.5 |
| 400 | 438.2 | 436.0 | 428.5 | 434.5 | 434.3 | 433.8 | 438.8 | 438.2 | 434.2 | 425.8 | 475.1 | 418.8 | 408.8 | 434.9 | 433.6 |
| | 26.2 | 26.0 | 38.0 | 30.9 | 30.9 | 30.8 | 30.5 | 30.6 | 30.6 | 30.3 | 6.4 | 6.3 | 13.7 | 30.8 | 30.7 |
| 800 | 867.8 | 860.7 | 846.3 | 857.6 | 858.9 | 858.2 | 862.8 | 864.3 | 860.6 | 845.3 | 917.7 | 834.8 | 822.4 | 859.0 | 857.6 |
| | 37.8 | 37.9 | 55.3 | 45.3 | 45.2 | 45.6 | 44.7 | 44.7 | 45.2 | 44.7 | 8.8 | 10.7 | 23.2 | 45.2 | 45.3 |

$\rho_{EXP}$ = expected mineral density, $\rho_{OBS}$ = observed mineral density.

observed mineral density ($\rho_{OBS}$), a multiple regression model was constructed with $\rho_{OBS}$ for 100, 200, 400, and 800 mg HA/cm³ phantom rods as dependent variable and energy (E), image resolution (RES), vial size (VS), beam hardening correction factor (CORR) and averaging (AVG) as predictor variables. The variables of E, VS, and AVG were coded as continuous variables, whereas RES and CORR were coded as categorical variables using dummy variables of CORR_700 (0,1) and CORR_1200 (0,1) and RES_MED (0,1) and RES_HIGH (0,1).

For Aim 2, in order to study the effect of each imaging condition on the $\rho_{OBS}$ for the total range of density (100 to 800 mg HA/cm³), a simple regression ($\rho_{EXP} = \rho_{OBS} \beta_1 + \beta_0$) was applied to $\rho_{EXP}$ and $\rho_{OBS}$ data for each imaging condition, which resulted in coefficients of determinations ($R^2$) of greater than 0.999 for all conditions. All predictors and interaction terms were entered into the model simultaneously, and model $R^2$ and significance were used to assess the predictability of each model. The $\beta$ coefficients and P values for the predictor and the slope ($\beta_1$) and intercept ($\beta_0$) of simple regression lines were reported individually.

For Aim 3, mineral densities obtained for 500, 1000 and 1500 mg HA/cm³ CIRS phantoms were analyzed as dependent variable and the effect of spatial configuration and surrounding densities were tested in four defined Cases (I–IV). One way analysis of variance (ANOVA) was used to compare mean observed mineral density of each phantom rod at three positions from the center to the periphery of the reconstruction space (Case I). Paired sample *t*-test was used to analyze the effect of changing surrounding densities on the observed mineral density of each phantom rod at the center (Case II) and periphery (Case III) of the reconstruction space and by changing the orientation of the object (Case IV) in the reconstruction space.

Data analysis was performed with the SPSS statistical software package (Versions 17.0, SPSS, Chicago, Illinois). For all analyses, two-tailed P values smaller than 0.05 were considered statistically significant.

## Results

The SCANCO calibration phantom was scanned over a period of 12 months and the observed variation in recorded mineral density was very small with coefficient of variation (CV) of <0.005. A substantial amount of variation was observed in density measurement of the same phantom as a result of changing imaging parameters (Table 2). The CV of $\rho_{OBS}$ ranged from 5.3 to 22.0% for 0 to 800 mg HA/cm³ phantoms. For the range of density that is covered by SCANCO calibration phantom, the relationship between $\rho_{OBS}$ and $\rho_{EXP}$ was fairly linear with $R^2$ values of greater than 0.99 for all 216 imaging conditions.

The effect of different imaging conditions on the $\rho_{OBS}$ was explored using multiple regression models based on parameters of energy level, vial diameter, resolution, beam hardening correction factor and averaging (Table 3). All models were significant (all P values<0.001) and highly predictive of observed density with $R^2$ ranging from 0.90 to 0.95. The beam hardening correction factor, energy level, and vial diameter were significant predictors of $\rho_{OBS}$ for all density ranges (all P values<0.001). The resolution and averaging were not significant predictors of density for most phantom densities and only showed significance for phantom rod of 0.0 mg HA/cm³ (P value>0.03 and 0.005 respectively). Based on standardized coefficients, which explain the relative contribution of each predictor to the model, beam hardening correction factor was the most important predictor of density. Individual standardized coefficients showed significant differences among all subcategories of beam hardening correction factor 200 vs. 700; 200 vs. 1200, and 700 vs. 1200 mg HA/cm³. The 200 vs. 1200 mg HA/cm³ difference demonstrated the largest contrast for all density ranges (standardized coefficient = 0.92–1.03, P value<0.001 for all cases).

In order to study the effect of imaging conditions on the relationship between $\rho_{OBS}$ and $\rho_{EXP}$, a linear regression line was applied to the data, and their intercepts ($\beta_0$) and slopes ($\beta_1$) were modeled based

**Table 3**
Multiple regression models of $\rho_{OBS}$ (for 0.0, 100.0, 200.0, 400.0, and 800.0 mg HA/cm³ SCANCO phantoms) and the Intercept ($\beta_0$) and Slope ($\beta_1$) of the $\rho_{OBS}$ vs. $\rho_{EXP}$ based on energy, vial diameter, resolution, bean hardening correction factor and Averaging. The Standardized Coefficients estimate relative contribution of each predictor into the model.

| | $\rho_{OBS}$ (mg HA/cm³) | | | | | | | | | | | | | | | | | | $\rho_{OBS}$ vs. $\rho_{EXP}$ (mg HA/cm³) | | | | | |
| | 0 | | | 100 | | | 200 | | | 400 | | | 800 | | | $\beta_0$ | | | $\beta_1$ | | |
| | $R^2$ | Std. Coeff. | P Value | $R^2$ | Std. Coeff. | P Value | $R^2$ | Std. Coeff. | P Value | $R^2$ | Std. Coeff. | P Value | $R^2$ | Std. Coeff. | P Value | $R^2$ | Std. Coeff. | P Value | $R^2$ | Std. Coeff. | P Value |
|---|---|---|---|---|---|---|---|---|---|---|---|---|---|---|---|---|---|---|---|---|---|
| Models | 0.90 | | 0.001* | 0.95 | | 0.001* | 0.94 | | 0.001* | 0.95 | | 0.001* | 0.94 | | 0.001* | 0.92 | | 0.001* | 0.93 | | 0.001* |
| Predictors: | | | | | | | | | | | | | | | | | | | | | |
| Energy (kVp) | | −0.42 | 0.001* | | −0.24 | 0.001* | | −0.06 | 0.001* | | −0.13 | 0.001* | | −0.20 | 0.001* | | 0.21 | 0.001* | | 0.17 | 0.001* |
| Vial diameter (mm) | | −0.17 | 0.001* | | −0.15 | 0.001* | | −0.16 | 0.001* | | −0.16 | 0.001* | | −0.14 | 0.001* | | 0.17 | 0.001* | | 0.15 | 0.001* |
| Resolution | | | | | | | | | | | | | | | | | | | | | |
| Low vs. medium | | 0.06 | 0.03* | | 0.01 | 0.62 | | 0.02 | 0.46 | | 0.01 | 0.86 | | −0.01 | 0.48 | | −0.04 | 0.10 | | 0.03 | 0.13 |
| Low vs. high | | 0.01 | 0.94 | | 0.02 | 0.20 | | 0.02 | 0.31 | | 0.01 | 0.53 | | −0.01 | 0.74 | | −0.04 | 0.10 | | 0.02 | 0.34 |
| Medium vs. high | | 0.05 | 0.04* | | 0.02 | 0.43 | | 0.01 | 0.78 | | 0.01 | 0.65 | | 0.01 | 0.71 | | 0.00 | 1.00 | | −0.01 | 0.58 |
| Beam hardening correction factor (mg HA/cm³) | | | | | | | | | | | | | | | | | | | | | |
| 200 vs. 700 | | 0.68 | 0.001* | | 0.82 | 0.001* | | 0.85 | 0.001* | | 0.87 | 0.001* | | 0.87 | 0.001* | | −0.78 | 0.001* | | −0.87 | 0.001* |
| 200 vs. 1200 | | 0.92 | 0.001* | | 1.01 | 0.001* | | 1.03 | 0.001* | | 1.02 | 0.001* | | 1.00 | 0.001* | | −1.02 | 0.001* | | −0.99 | 0.001* |
| 700 vs. 1200 | | 0.24 | 0.001* | | 0.20 | 0.001* | | 0.18 | 0.001* | | 0.15 | 0.001* | | 0.13 | 0.001* | | −0.24 | 0.001* | | −0.12 | 0.001* |
| Averaging (No. images) | | −0.06 | 0.005* | | −0.02 | 0.36 | | −0.03 | 0.11 | | −0.02 | 0.17 | | −0.02 | 0.35 | | 0.04 | 0.03* | | 0.01 | 0.65 |

$\rho_{EXP}$ = expected mineral density, $\rho_{OBS}$ = observed mineral density, Std. Coeff = Standardized Coefficient, , $\beta_0$ = intercept, , $\beta_1$ = slope, *Statistically Significant

on the same imaging parameters using multiple regression. Both models were significant (P values<0.001) and explained more than 92% of the variability in the slope and intercept of the relationship between $\rho_{OBS}$ and $\rho_{EXP}$ (Table 3). Beam hardening correction factor, energy and vial diameter were significant predictors of both $\beta_0$ and $\beta_1$ intercept (P values<0.001), while averaging was only a significant predictor of $\beta_0$ (P value = 0.03).

A series of density correction curves were generated based on observed mineral densities for 0, 100, 200, 400 and 800 mg HA/cm$^3$ phantoms for every combination of energy, vial diameter and beam hardening correction factor. The slope ($\beta_0$) and intercept ($\beta_1$) of these 36 curves (Table 4) can be used to calculate $\rho_{EXP}$ from $\rho_{OBS}$ for phantoms imaged using the SCANCO system.

We used CIRS phantoms to study the effect of spatial configuration and surrounding densities on $\rho_{OBS}$ and Cases I through IV representing common imaging scenarios. Varying the location of the object within the reconstruction space from the center to the periphery (three positions) resulted in changes of up to 10% in the $\rho_{OBS}$ (P<0.005 for all density rods) (Table 5 — Case I). Presence of surrounding densities also had a significant effect on the $\rho_{OBS}$ at the center of the reconstruction space (P<0.001 for all density rods). All phantom rods, at the center of the reconstruction space, reported lower mineral densities of up to 17% in the presence of surrounding phantom rods (Table 5 — Case II). A similar effect was also observed, where phantoms rods at the periphery of the reconstruction space reported lower mineral density values of up to 14% when surrounded by other phantom rods (Table 5 — Case III). Changing the orientation

of an object inside the reconstruction space also had a significant effect on the $\rho_{OBS}$ (P<0.001 for all density rods, Table 5 — Case IV), resulting in a net change of up to 16% in the reported mineral density of the same region.

## Discussion

Micro-computed tomography is widely used in preclinical studies, and μCT-based mineral density is a commonly reported surrogate for bone strength in the literature ([8–10]). The non-destructive nature of this technique, allowing for repeated measurements of 3D bone indices, has lead to its popularity among researchers. However, differences in imaging protocols and sample configurations could potentially lead to erroneous results. Therefore, gaining insight into the factors that affect mineral density measurements by these systems has become increasingly important. This study evaluates the effect of different imaging parameters on the observed mineral density by μCT and provides statistical models to correct the offset in density measurements. Also, the effect of spatial configurations of specimens in the reconstruction space is studied using four common imaging scenarios, and resultant practical recommendations to reduce errors in density have been provided.

Our results indicate beam hardening correction factor, energy level and vial diameter as significant predictors of $\rho_{OBS}$. The manufacturer provides three levels of beam hardening correction factors for density measurements: 200, 700, and 1200 mg HA/cm$^3$ with all three levels displaying significant differences with one another. Fajardo et al. (2009)

**Table 4**
Density correction curves for 36 image conditions based on energy, beam hardening correction factor, and vial diameter and the intercept ($\beta_0$) and slope ($\beta_1$) of the linear regression of the observed and expected density ($\rho_{EXP} = \beta_1\,\rho_{OBS} + \beta_0$) for SCANCO phantoms.

| | Energy (kVp) | Vial diameter (mm) | Beam hardening correction factor (mg HA/cm$^3$) | $\rho_{EXP}$ 0 | 100 | 200 | 400 | 800 | $\beta_0$ | $\beta_1$ |
|---|---|---|---|---|---|---|---|---|---|---|
| $\rho_{OBS}$ | 70 | 16.4 | 200 | −23.18 | 102.67 | 247.21 | 484.50 | 926.10 | 6.90 | 1.18 |
| | | | 700 | −37.30 | 72.78 | 202.10 | 419.62 | 832.11 | 26.08 | 1.09 |
| | | | 1200 | −42.97 | 61.04 | 184.78 | 395.16 | 797.14 | 34.68 | 1.05 |
| | | 20.5 | 200 | −26.62 | 101.26 | 245.92 | 483.63 | 926.20 | 8.95 | 1.19 |
| | | | 700 | −40.89 | 71.54 | 201.13 | 418.66 | 831.59 | 28.11 | 1.09 |
| | | | 1200 | −46.40 | 60.43 | 184.52 | 395.08 | 797.87 | 36.36 | 1.05 |
| | | 30.7 | 200 | −26.55 | 99.45 | 242.78 | 479.47 | 923.33 | 10.14 | 1.18 |
| | | | 700 | −40.28 | 69.86 | 198.18 | 414.66 | 828.27 | 29.13 | 1.08 |
| | | | 1200 | −45.73 | 58.52 | 181.57 | 390.97 | 793.92 | 37.45 | 1.05 |
| | | 36.9 | 200 | −28.92 | 95.25 | 235.16 | 470.40 | 906.54 | 12.65 | 1.17 |
| | | | 700 | −41.86 | 66.09 | 191.27 | 406.40 | 812.69 | 31.63 | 1.07 |
| | | | 1200 | −47.24 | 55.04 | 174.84 | 383.34 | 779.47 | 40.06 | 1.03 |
| | 55 | 16.4 | 200 | −23.11 | 101.53 | 241.18 | 476.66 | 919.05 | 8.30 | 1.17 |
| | | | 700 | −33.36 | 77.88 | 204.84 | 423.82 | 842.53 | 23.14 | 1.09 |
| | | | 1200 | −33.91 | 77.20 | 203.54 | 421.97 | 840.24 | 23.78 | 1.09 |
| | | 20.5 | 200 | −25.18 | 100.56 | 240.34 | 475.80 | 918.72 | 9.58 | 1.18 |
| | | | 700 | −35.37 | 77.19 | 204.15 | 422.98 | 842.25 | 24.34 | 1.10 |
| | | | 1200 | −35.80 | 76.29 | 202.82 | 421.42 | 840.07 | 25.00 | 1.09 |
| | | 30.7 | 200 | −25.59 | 98.65 | 236.87 | 471.26 | 914.24 | 10.90 | 1.17 |
| | | | 700 | −35.81 | 75.22 | 200.89 | 418.68 | 836.90 | 25.70 | 1.09 |
| | | | 1200 | −36.28 | 74.38 | 199.79 | 416.92 | 834.65 | 26.32 | 1.09 |
| | | 36.9 | 200 | −27.55 | 95.43 | 230.20 | 462.73 | 898.22 | 12.84 | 1.15 |
| | | | 700 | −37.34 | 72.25 | 194.61 | 410.60 | 821.76 | 27.74 | 1.07 |
| | | | 1200 | −37.64 | 71.37 | 193.44 | 408.71 | 819.52 | 28.36 | 1.07 |
| | 45 | 16.4 | 200 | −22.19 | 102.42 | 236.81 | 477.37 | 921.49 | 8.89 | 1.18 |
| | | | 700 | −30.42 | 80.56 | 199.83 | 427.17 | 843.79 | 22.17 | 1.09 |
| | | | 1200 | −35.61 | 74.78 | 193.40 | 422.78 | 843.11 | 27.85 | 1.10 |
| | | 20.5 | 200 | −22.34 | 102.07 | 237.06 | 478.20 | 925.46 | 9.43 | 1.18 |
| | | | 700 | −29.84 | 80.92 | 202.56 | 426.15 | 849.23 | 21.97 | 1.10 |
| | | | 1200 | −35.01 | 75.13 | 196.91 | 421.66 | 847.50 | 27.33 | 1.10 |
| | | 30.7 | 200 | −22.85 | 100.02 | 235.15 | 474.73 | 923.63 | 10.73 | 1.18 |
| | | | 700 | −30.30 | 78.93 | 201.12 | 422.49 | 845.46 | 23.04 | 1.10 |
| | | | 1200 | −35.53 | 73.04 | 195.27 | 418.20 | 844.59 | 28.58 | 1.10 |
| | | 36.9 | 200 | −25.13 | 97.14 | 229.90 | 466.25 | 908.87 | 12.51 | 1.17 |
| | | | 700 | −32.51 | 76.30 | 195.93 | 413.96 | 830.66 | 25.01 | 1.08 |
| | | | 1200 | −37.88 | 70.57 | 190.15 | 409.80 | 830.15 | 30.65 | 1.09 |

$\rho_{EXP}$ = expected mineral density, $\rho_{OBS}$ = observed mineral density.

**Table 5**
Observed density values of the CIRS phantoms for Cases I, II, III and IV. Images were obtained under conditions of tube voltage = 55 kVp, tube current = 114 μA, integration time = 250 ms, isotropic voxel size = 0.020 mm (vial size = 20.5 mm), and beam hardening correction factor = 700.

| $\rho_{EXP}$ (mg HA/cm$^3$) | Spatial configurations | $\rho_{OBS}$ (mg HA/cm$^3$) | | | | | | |
|---|---|---|---|---|---|---|---|---|
| | | Center | | Middle | | Periphery | | |
| | | Mean | Std. Dev. | Mean | Std. Dev. | Mean | Std. Dev. | P value |
| 500 | Case I | 511.51 | 0.13 | 507.48 | 0.7 | 501.33 | 0.68 | 0.001 [*] |
| 1000 | | 972.53 | 0.51 | 972.75 | 0.41 | 961.19 | 1.51 | 0.003 [*] |
| 1500 | | 1352.4 | 0.76 | 1352.8 | 0.55 | 1340 | 0.86 | 0.005 [*] |

| $\rho_{EXP}$ (mg HA/cm$^3$) | | Center | | Center + surrounding | | P value |
|---|---|---|---|---|---|---|
| | | Mean | Std. Dev. | Mean | Std. Dev. | |
| 500 | Case II | 511.51 | 0.13 | 462.7 | 0.4 | 0.001 [*] |
| 1000 | | 972.53 | 0.51 | 900.4 | 1.58 | 0.001 [*] |
| 1500 | | 1352.4 | 0.76 | 1250 | 3.28 | 0.001 [*] |

| $\rho_{EXP}$ (mg HA/cm$^3$) | | Periphery | | Periphery + Surrounding | | P value |
|---|---|---|---|---|---|---|
| | | Mean | Std. Dev. | Mean | Std. Dev. | |
| 500 | Case III | 501.33 | 0.68 | 451.1 | 0.19 | 0.001 [*] |
| 1000 | | 961.19 | 1.51 | 862.3 | 0.04 | 0.001 [*] |
| 1500 | | 1340 | 0.86 | 1290 | 0.34 | 0.001 [*] |

| $\rho_{EXP}$ (mg HA/cm$^3$) | | Vertical orientation | | Horizontal orientation | | P value |
|---|---|---|---|---|---|---|
| | | Mean | Std. Dev. | Mean | Std. Dev. | |
| 500 | Case IV | 511.51 | 0.13 | 498.3 | 0.67 | 0.001 [*] |
| 1000 | | 972.53 | 0.51 | 915.4 | 0.37 | 0.001 [*] |
| 1500 | | 1352.4 | 0.76 | 1266 | 0.86 | 0.001 [*] |

$\rho_{EXP}$ = expected mineral density, $\rho_{OBS}$ = observed mineral density, [*] Statistically significant.

reported 20.1% errors in accuracy of $\rho_{OBS}$ for 200 mg HA/cm$^3$ beam hardening correction factors [6] , while the error was 17.2% for the 1200 mg HA/cm$^3$ beam hardening correction factor. Kazakia et al. studied the cupping artifact by comparing the X-ray attenuation between inner and peripheral regions of cylindrical samples. They observed that using the 200 mg HA/cm$^3$ beam hardening correction factor resulted in the largest discrepancy (mean difference of $46.7 \pm 3.3$ mg HA/cm$^3$) in $\rho_{OBS}$ [2], while the 1200 mg HA/cm$^3$ correction reduced the discrepancy to less than half. Overall, the beam hardening correction factor is the most important predictor of $\rho_{OBS}$. Therefore, it is important to optimize its effect across different range of density values and imaging parameters. Although using current beam hardening correction factors improves mineral density measurements, a residual error still remains in place. The proposed density correction curves (Appendix B) will take into account the errors associated with different levels of energy, vial size and beam hardening correction factor and will further improve the density measurements.

There are a number of limitations that need to be taken into account in interpretation of our results. First, we used calibration phantoms to study the effect of different imaging conditions on the observed mineral density in bone. This may not completely represent the geometry and shape of all bone samples that are imaged by μCT. Also, two sets of phantoms were used in this study. The standard calibration phantom (SCANCO) which is embedded in resin was used to study the effect of imaging conditions, and a custom-made phantom (CIRS), surrounded by distilled water, was used to study the effect of spatial configuration of phantoms. This may not be as important, since each phantom is used to study a different aim with the ultimate goal of demonstrating differences between observed and expected densities under different conditions. Also, we used the Scanco μCT 40 system for this study, and although all polychromatic μCT systems follow similar imaging principals, our results need to be validated across different platforms to be generalized to all available imaging systems.

As μCT imaging provides a much smaller voxel size, more of the actual HA crystals are being imaged (as opposed to being averaged

out by the surrounding tissue), resulting in reporting of increased density values than obtained by lower resolution clinical CT scanners. Additionally, bone samples commonly used in research span the species range (mouse, rat, human both fetal and adult, cow, whale …) which report a density range of 550 to 750 mg HA/cm$^3$ for cancellous and 800 to ~1300 mg HA/cm$^3$ for cortical bones (Fig. 1). When the observed mineral density values for higher range of densities are extrapolated from the actual values for both SCANCO and CIRS phantoms, the resultant extrapolated values diverge from the expected mineral density values (Fig. 3). For instance, for an expected mineral density of 1750 mg HA/cm$^3$, CIRS and SCANCO phantoms will report observed mineral density values of 1899 mg HA/cm$^3$ and 1518 mg HA/cm$^3$, resulting in mineral density underestimations of 13.2% for CIRS and overestimation of 8.5% for SCANCO phantom. The $\rho_{OBS}$ and $\rho_{EXP}$ had a fairly linear relationship for both SCANCO, and CIRS phantoms in our experiment, but there are reports [11,12] that indicate non-linear bean hardening artifact in higher density ranges, which could be another source of error for density extrapolation based on a density range that only spans up to 800 mg HA/cm$^3$. Therefore, including a higher range of calibration density will provide useful information about the nature and extent of error at any given density level. Overall, the SCANCO phantom provides a more accurate estimation of the mineral density values than the in house assembled CIRS phantom.

Physical constraints in manufacturing solid HA phantoms with high density ranges lead to the introduction of liquid phantoms which generate more homogeneous cross-sections and can reach mineral density value of 1000–1100 mg.cm$^{-3}$. Issues with maintenance of these phantoms such as precipitation of crystals at high doses and air bubble formation make these phantoms less practical. Recently, Scheizer et al. have generated calibration curves with range of density from 100 to 3000 mg.cm$^{-3}$ by compacting of raw HA under different pressures [13]. Findings from their work will resolve data extrapolation problem resulting from lower range conventional calibration curves and will introduce phantoms with more uniform distribution of HA across the surface.
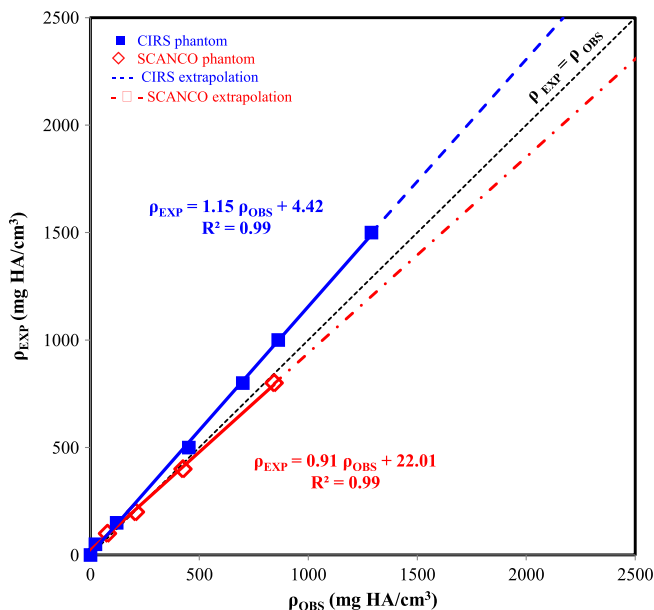
**Fig. 3.** Observed and expected mineral density for CIRS and SCANCO phantoms. Based on extrapolation of mineral density from actual values, deviation of the observed mineral density is more prominent for CIRS phantoms than SCANCO.

Combining the results of this study with the authors' previous study, performed on the same set of phantoms to investigate the effects of varying imaging parameters on the mineral density [3], we conclude that tube voltage (energy), surrounding media, resolution (comprised of object to source distance and detector size), and beam hardening correction factors significantly affect the relationship between X-ray attenuation in µCT. Any µCT based mineral density measurement with known imaging configuration can be corrected using this family of curves to optimize the final density output. This can be easily incorporated into the current imaging software as a simple post-processing step.

The effect of spatial variation of the specimens within the reconstruction space on their X-ray attenuation coefficient values has been studied before. Mulder et al. showed that the X-ray attenuation coefficient values were higher in specimens with smaller diameters [12]. A detailed study by Fajardo et al. on the effect of specimen size on the µCT-based mineral density measurements revealed that size and porosity can introduce errors into density measurements [6].

This study has explored the effects of spatial variation of a sample within the reconstruction space and the presence/absence of surrounding densities on the X-ray attenuation in µCT. Changing the phantom location from the center to the periphery of the reconstruction space resulted in a significant drop in the recorded attenuation coefficient values, as the reconstruction algorithm is optimized to work for an object at the center of the reconstruction space. Additionally, presence of surrounding densities in the reconstruction space caused a significant drop in the attenuation coefficient values of the object under investigation both at the center and the periphery of the reconstruction space.

There are a number of implications for the findings presented in this study. First, imaging configurations should be selected with the knowledge of parameters that can affect the density measurement in µCT. In order to minimize errors associated with spatial configuration of the specimens within the reconstruction space, specimens should be either at the center or at the same distance from the center of the reconstruction space. Since presence of surrounding densities affect the X-ray attenuation of an object, the orientation (for scanning long bones), location and geometry of a specimen should be taken into account. Authors have provided the coefficients for all correction curves (Table 2) which will be available online for use as a starting point. As one is not aware of the distribution of the mass of an object to be scanned *apriori*, it is difficult to provide a correction starting point. To that end, iterative reconstruction schemes could be introduced to fine tune the final reconstruction after a first initial guess on the geometry of the object has been made using standard convolution-back projection and possible first order beam hardening correction measures.

In conclusion, this study follows up on the authors' initial investigations of the imaging settings and spatial configurations that may affect generated mineral density measurements. A family of correction curves for the SCANCO system has been generated using calibration phantoms provided by the manufacturer, providing new insight into the sources of error in µCT based density measurements. Using the same approach, more specific correction curves can be generated for a particular density range and imaging platform and implemented as a sub-routine in the density measurements. Finally, some concerns regarding the spatial configuration and positioning of objects within the reconstruction space have been addressed in this study. The current project in tandem with the recent publications in the field open the possibility of designing a universal calibration phantom which takes into account the homogeneity of the material, density range, size and the location of the densities which will allow the researchers to compare density values generated by different µCT systems using different imaging settings.

## References

[1] Kak AC, Slaney M, IEEE Engineering in Medicine and Biology Society. Principles of computerized tomographic imaging. New York: IEEE Press; 1988.
[2] Kazakia GJ, Burghardt AJ, Cheung S, Majumdar S. Assessment of bone tissue mineralization by conventional x-ray microcomputed tomography: comparison with synchrotron radiation microcomputed tomography and ash measurements. Med Phys 2008;35:3170–9.
[3] Nazarian A, Snyder BD, Zurakowski D, Muller R. Quantitative micro-computed tomography: a non-invasive method to assess equivalent bone mineral density. Bone 2008;43:302–11.
[4] Burghardt AJ, Kazakia GJ, Laib A, Majumdar S. Quantitative assessment of bone tissue mineralization with polychromatic micro-computed tomography. Calcif Tissue Int 2008;83:129–38.
[5] Deuerling JM JRD, Niebur GL, Roeder RK. Cortical bone mineralization measured by quantitative micro-computed tomography using a non-linear calibration of attenuation and mineral density. Trans Ortho Res Soc. Las Vegas, NV; 2009. p. Poster No. 2145.
[6] Fajardo RJ, Cory E, Patel ND, Nazarian A, Laib A, Manoharan RK, Schmitz JE, DeSilva JM, MacLatchy LM, Snyder BD, Bouxsein ML. Specimen size and porosity can introduce error into µCT-based tissue mineral density measurements. Bone 2009;44(1):176–84.
[7] Burghardt A, Kazakia G, Laib A, Saldanha K, Majumdar S. Quantitative assessment of bone tissue mineralization with polychromatic micro-computed tomogrpahy. Journal of Bone and Mineral ResearchNashville, TN: American Society for Bone and Mineral Research; 2005. p. S330.
[8] Gustafsson BI, Tommeras K, Nordrum I, Loennechen JP, Brunsvik A, Solligard E, et al. Long-term serotonin administration induces heart valve disease in rats. Circulation 2005;111:1517–22.
[9] Boyd SK, Szabo E, Ammann P. Increased bone strength is associated with improved bone microarchitecture in intact female rats treated with strontium ranelate: a finite element analysis study. Bone 2011;48:1109–16.
[10] Gabet Y, Muller R, Levy J, Dimarchi R, Chorev M, Bab I, et al. Parathyroid hormone 1–34 enhances titanium implant anchorage in low-density trabecular bone: a correlative micro-computed tomographic and biomechanical analysis. Bone 2006;39:276–82.
[11] Deuerling JM, Rudy DJ, Niebur GL, Roeder RK. Improved accuracy of cortical bone mineralization measured by polychromatic microcomputed tomography using a novel high mineral density composite calibration phantom. Med Phys 2010;37: 5138–46.
[12] Mulder L, Koolstra JH, Van Eijden TM. Accuracy of microCT in the quantitative determination of the degree and distribution of mineralization in developing bone. Acta Radiol 2004;45:769–77.
[13] Schweizer S, Hattendorf B, Schneider P, Aeschlimann B, Gauckler L, Muller R, et al. Preparation and characterization of calibration standards for bone density determination by micro-computed tomography. Analyst 2007;132:1040–5.